Unsteadiness in a Compressible Reattaching Shear Layer

Akshay S. Deshpande* and Jonathan Poggie†
Purdue University, West Lafayette, IN 47904-2045, USA

Shock-Wave/Boundary-Layer interactions are characterized by large-scale, low frequency unsteadiness which often results in severe aerothermal loads and structure fatigue on a high-speed vehicle. In this study, unsteadiness in a compressible reattaching shear layer is investigated by analyzing results from a delayed detached eddy simulation (DDES) carried out by Leger et al. (2017). The shear layer is generated by a Mach 2.9 turbulent boundary layer separating on a backward facing step, and reattaching on a 20 deg ramp. The integration times were long enough to capture the low-frequency oscillations of the reattachment shock. The time-mean results agreed well with experimental data after accounting for an over-prediction of the flow turning angle. Low frequency flapping motion of the shear layer, as well as large spanwise vortex structures, were observed in the computational data. These two features are investigated in detail using correlations, signal analysis, and conditional averaging.

Nomenclature

C_{DES}	DES length scale parameter
D	Step height (m)
$G(f)$	Spectral density function (Pa^2s)
L	Cavity length (m)
M_c	Convective Mach number
R	Correlation magnitude
T	Temperature (K)
f	Frequency (Hz)
p	Pressure (Pa)
t	Elapsed time (s)
u	Streamwise velocity component (m/s)
v	Wall–normal velocity component (m/s)
w	Spanwise velocity component (m/s)
x, y, z	Cartesian coordinate system (m)
$\delta_\circ$	Incoming boundary layer thickness (m)
μ	Kinematic viscosity ($kgm^{-1}s^{-1}$)
ρ	Density (kg/m^3)
σ_p	RMS of pressure fluctuations (Pa)
τ_{int}	Integral time scale (s)
Superscripts:	
$'$	Fluctuating quantities
$\tilde{}$	Instantaneous quantities
$+$	Inner coordinates
Subscripts:	
∞	Freestream quantities
w	Wall quantities
R	Quantities at the mean reattachment location

*Graduate Research Assistant, School of Aeronautics and Astronautics, 701 W. Stadium Avenue. AIAA Student Member.
†Associate Professor, School of Aeronautics and Astronautics, 701 W. Stadium Avenue. AIAA Associate Fellow.

I. Introduction

Shock-wave boundary layer interactions tend to be inherently unsteady, characterized by a wide range of frequencies ranging from those present in the upstream boundary layer, to the ones which are lower by an order of magnitude or more [1]. The low frequencies are dominant in a power spectrum obtained in the intermittent region of the interaction, and correspond to the oscillations of the shock foot. Exhaustive research has been carried out on the origin of the large scale, low-frequency motions [1–3], and the general consensus is that the low frequency separation bubble unsteadiness is characterized by a weakly–damped global mode, sensitive to external perturbations with matching scales [4–6]. The canonical interactions investigated consist of a compression ramp, impinging-reflected shock and three-dimensional geometries such as blunt and sharp-fins. But there is a dearth of research carried out unsteadiness in a compressible reattaching shear layer.

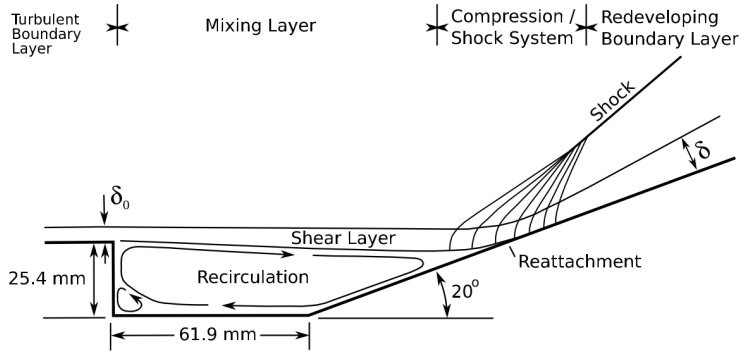

Fig. 1 Mean-flowfield [7] (Reprinted with permission from the author).

Reattaching shear layers occur in practical applications such as engine exhaust reattaching onto a surface, cavity flameholders, or an open bay for store release in an aircraft [7, 8]. The mean flowfield is shown in Fig. 1. This flow configuration has a distinct advantage of a fixed separation point unlike other canonical geometries such as ramps and fins. The reattachment shock in this case undergoes a similar large scale, low-frequency motion, which causes fatigue loading on an aircraft. Experimental measurements of mean and turbulent quantities in the shear layer were obtained by Settles et al. [9] and Hayakawa et al. [10]. Settles at al. [9] observed mean-flow similarity and constant growth rate in the free shear layer after about 18 boundary layer thicknesses after separation. A dramatic increase in turbulence intensity was noted by Hayakawa et al. [10] near the reattachment point, in addition to changes in turbulent length scales. Near reattachment, the boundary layer is highly distorted, but eventually relaxes towards an equilibrium turbulent boundary layer profile. An experiment on the unsteadiness of reattaching shear layer carried out by Poggie et al. [11] indicates the role of upstream mechanisms in separation unsteadiness. They introduced disturbances in the upstream boundary layer, which increased the intensity of pressure fluctuations and amplitude of the shock motion, as well as displayed a distinct shift towards lower frequencies in the power spectra. Large scale flapping of shear layer about the separation point, coherent structures in the mixing layer, or a combination of both are possible sources of reattachment unsteadiness.

Eaton and Johnston [12, 13] performed an experiment on a backward facing step in a low speed air flow facility. The flow was incompressible and the separated flow reattached on the cavity wall. They observed shear layer flapping motion with time scales several times longer than the largest turbulent eddies, which caused a broad movement of the reattachment point. The authors attribute the flapping motion to an instantaneous imbalance between shear-layer entrainment from the recirculating zone and re-injection of fluid near the reattachment point. Ma and Schröder [14] carried out an SVD (Singular Value Decomposition) and POD (Proper Orthogonal Decomposition) analysis of a backward facing step flow at a Reynolds number of 2×10^4. They concluded that the onset of flapping motions were induced by the maximum reverse flow region, located in the middle part of the reattachment length. The flapping motions feed back to the reverse flow region, resulting in change of the recirculating region.

In case of a compression ramp interaction, Ganapathisubramani et al. [15, 16] noted the presence of superstructures (about 40 boundary layer thicknesses long) in the logarithmic region of the boundary layer. These structures correlated well with the instantaneous separation line as well as accounted for the lower frequencies in the spectra of shock foot motion. In this study, influence of upstream structures in the mixing layer on the reattachment shock unsteadiness is worth investigating. From the work of Brown and Roshko [17], it is known that the mixing layer consists of large

coherent spanwise structures which result from a Kelvin-Helmholtz instability. These structures grow in size downstream until vortex stretching causes breakdown to fine-scale turbulence. In addition to the spanwise vortices, Bernal and Roshko [18] discovered secondary streamwise vortices which originate from an internal instability of the primary vortices. They proposed a model for the vortex topology as shown in Fig. 2.

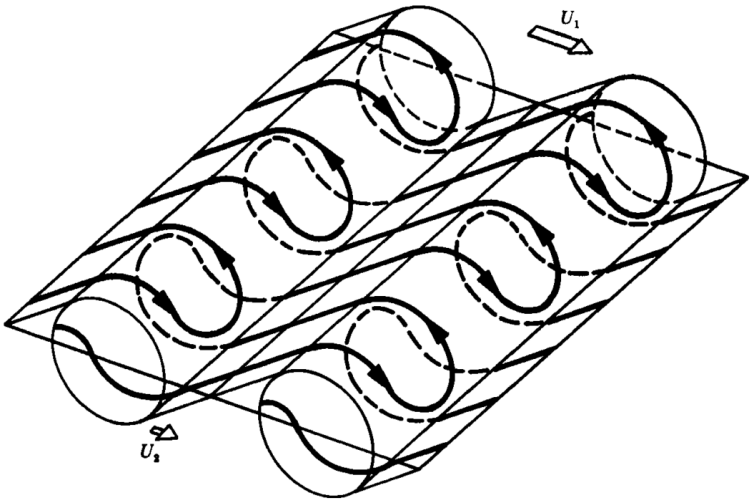

Fig. 2 Vortex topology [18] (under Cambridge University Press permission for use of a single figure).

The streamwise vortex lines shown in bold and dotted lines loop back and forth around the spanwise rollers and occur in counter-rotating pairs. The authors suggest that these pairs join to form hairpin configuration downstream. Dimotakis and Brown [19] investigated the dynamics of mixing layer at high Reynolds numbers up to 3×10^6. The large spanwise structures found in Brown and Roshko's experiments were found to persist at high Reynolds numbers, though with different flow dynamics. Samimy et al. [20] used space-time correlations to study compressibility effects on large structures in mixing layers. Their results indicated a horseshoe type vortex with its head at the low speed side and inclined in both $x - y$ and $x - z$ planes. The current study aims to investigate the structure of the flowfield and focus on the unsteady aspects of the shear–layer flapping.

II. Methodology

The data presented in this study were obtained from the calculations carried out by Leger et al. [7]. Only a few details will be discussed in this section. OVERFLOW 2.2K, an overset grid computational fluid dynamics solver developed by NASA was used to carry out delayed detached-eddy simulations (DDES). The calculations involved a hybrid RANS/LES approach. The test geometry (see Fig. 1) consisted of a backward facing step 25.4 mm high with a cavity extending 61.9 mm, followed by a 160 mm long ramp inclined at 20 deg. The flow conditions are given in Table. 1.

Table 1 Flow conditions.

Parameter	Value
u_∞	572 m/s
ρ_∞	0.77 kg/m^3
T_∞	95 K
T_w	266 K
$\rho_\infty u_\infty / \mu_\infty$	67×10^6 m^{-1}
M_∞	2.92
M_c	1.1
$\delta_\circ$	3 mm

In the above table, M_c is the convective Mach number and $\delta_\circ$ is the incoming boundary layer thickness. A uniform velocity profile was imposed at the inlet. An extrapolation condition was used on the top surface and outlet. A periodic boundary condition was set on the spanwise boundaries. The wall was maintained at constant temperature T_w with the no-slip condition. The DDES computation was run with a time step of $\Delta t = 0.25\,\mu s$ and three sub-iterations, for a total of 2×10^6 iterations. This amounts to a total of 0.5 s of physical time, sufficient to capture the low frequency unsteadiness of the interaction. Additional details on how the time step and domain width were chosen can be found in Ref. [7].

The grid used in the computations was divided into three regions: region upstream of the step corner (I), cavity region (II), and region above the cavity (III). Section I, II, and III consisted of $191 \times 129 \times 321$, $1669 \times 161 \times 321$, and $1669 \times 129 \times 321$ points. Overall, the grid consisted about 1.6×10^8 points. At the wall, Δy^+ was maintained ≤ 1. This corresponds to an initial grid spacing of $\Delta y = 1.7\,\mu$m. The grid was stretched to form a sponge layer at the side and top boundaries to minimize spurious wave reflections. Streamwise clustering was done close to the step to resolve the vortex roll–up due to Kelvin–Helmholtz instability, and near the ramp ends to accurately capture the flow turning. Additionally, wall–normal clustering was done in the shear layer region. The grid spacing in the spanwise direction was uniform.

For the calculations, a boundary layer profile computed by matching the momentum thickness from the experiments [9, 10] was imposed at the inlet. RANS calculations were carried out initially using the SA turbulence model and a converged solution was obtained after 60,000 iterations. The converged RANS solution was used as the initial condition for the DDES calculations. The DDES model was Spallart–Allmaras (SA) based with C_{DES} as the only adjustable parameter to determine the DES length scale. This parameter was set to 0.65 for the computations.

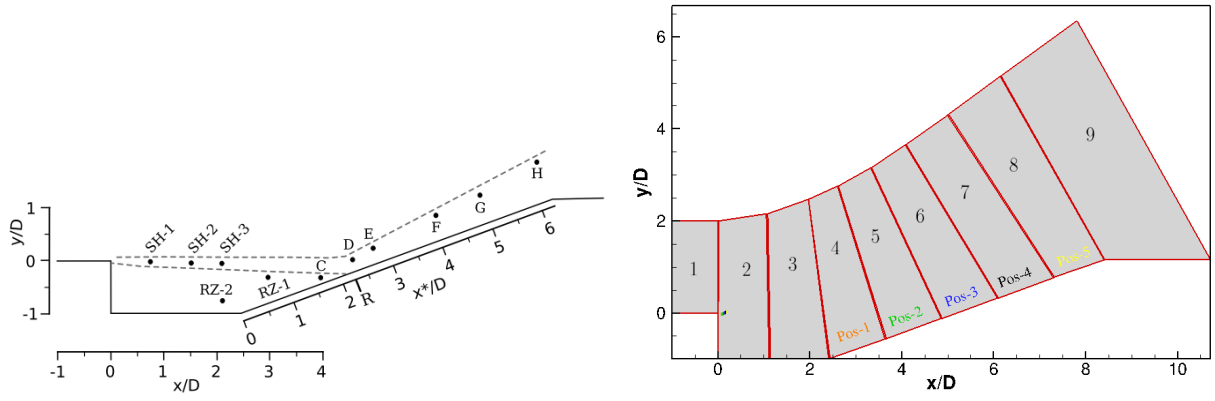

(a) Sampling stations [7] (Reprinted with permission from the author).

(b) Division of grid on the centerplane.

Fig. 3 Extracted data locations.

Figure 3(a) shows the different sampling stations used to gather the data that was used for this analysis. The stations labeled in Fig. 3(a) are spanwise lines saved at every iteration. This corresponds to a sampling frequency of $f_s = 4$ MHz. Streamlines along the ramp surface at seven equidistant spanwise locations and at the first grid point off the wall were also sampled at the same frequency. The spanwise centerplane (at $z/D = 0$) was saved every 10 iterations ($f_s = 400$ kHz). The centerplane was divided into nine slices as shown in Fig. 3(b). The boundaries of five slices on the ramp (slices 4–8) coincide with the boundaries of the wall streamlines lying along the ramp center (i.e. at $k = 161$). These five different locations are also highlighted in Fig. 3(b) and labelled as *pos*–#. Henceforth, data used from the centerplanes and lines along the ramp will be referred to as slice–# and position–#. The naming convention for spanwise lines will be used as is in Fig. 3(a).

III. Results

This section initially discusses the mean and instantaneous flowfields, followed by a detailed analysis of the unsteadiness. The mean flowfield was obtained by averaging about 2×10^6 time–steps of the centerplane after eliminating the initial transients. Three-dimensional flow organization of the instantaneous flowfield is also presented.

A. Mean and instantaneous flow features

Figure 4 shows the mean density and velocity contours, non–dimensionalized by their respective freestream values. The coordinate axes are non–dimensionalized by the step height $D = 0.0254$ m. The separated shear layer layer curves downwards over the recirculating region shown in Fig. 4(a), before attaching on the ramp. Compression waves close to the ramp surface are observed as a result of flow turning due to the shear layer curvature, upstream of the time–mean reattachment point $x_R \approx 4.764D$. These compression waves coalesce to form a sharp reattachment shock in the freestream. A weak shock wave originating at the separation point borders the sound waves radiated from the shear layer, which are washed out in the averaging process.

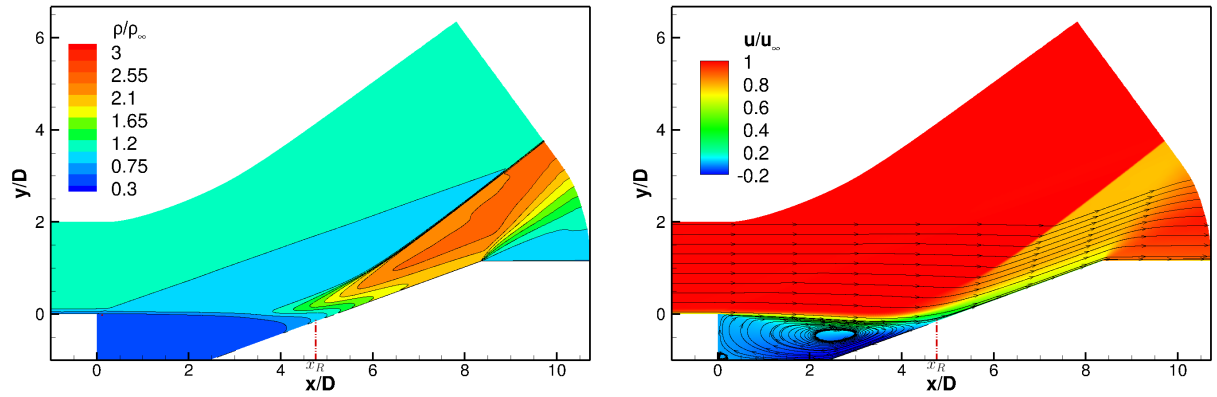

(a) Mean density contours.

(b) Mean u–velocity contours.

Fig. 4 Time–mean results.

The streamlines are superimposed on the mean streamwise velocity contours in Fig. 4(b). In addition to the massive separation vortex, a smaller corner vortex at the bottom of the step $(x/D, y/D) = (0, -1)$ is also visible. The flow accelerates across an expansion fan at the ramp corner. Settles et al. [9] observed self–similar mean velocity profiles after a distance of $18\delta_\circ$. The mean flow was two–dimensional in their experiments, which is consistent with the spanwise pressure distributions on the ramp from the computations.

Figure 5 shows the contours of the resolved Reynolds stresses. In this figure, $\langle\rangle$ represents root mean square (rms) of the quantity. All the three components of normal Reynolds stresses (in Figs. 5(a)– 5(c)) are qualitatively similar. The streamwise component (R_{11}) is highest in magnitude, followed by the spanwise component (R_{33}) and the wall-normal component (R_{22}) respectively. The Reynolds shear stress (R_{12}) is the lowest in magnitude. The fluctuations u', v' in Fig. 5(d) are negatively correlated in the mixing layer and the reattachment region, which is characteristic of turbulent transport by eddies. The time–mean reattachment location is marked by the red dashed line at $x_R \approx 4.764D$. The resolved Reynolds stresses begin to amplify prior to the reattachment location due to compression waves. As noted in the experiments of Hayakawa et al. [10], the Reynolds stresses continue to increase downstream of the reattachment location unlike subsonic reattaching boundary layers, wherein they peak at the reattachment location and decay downstream of it. Hayakawa et al. [10] attribute this behavior to the mean dilation rate after carrying out an analysis of the turbulent kinetic energy equation.

The instantaneous density plot on the centerplane ($z/D = 0$) is shown in Fig. 6. The contours are displayed in grayscale to resemble a typical planar laser scattering image [11]. At the separation point, the Kelvin-Helmholtz instability results in the formation of vortices which are uniform in the spanwise direction. Farther downstream, these vortices merge to form larger eddies. Based on the cross–correlation between the spanwise lines at $SH - 2$ and $SH - 3$ (see Fig. 3(a)), the average convection velocity of the large–scale turbulent structures was determined to be $u_c \approx 0.78u_\infty$. Additionally, smaller scale structures are generated. Sound waves emanating from the eddies in the shear layer can be visualized clearly. The redeveloping boundary layer on the ramp is characterized by eddies which are inclined at an angle of about 45° with respect to the ramp surface. Sound waves radiated from these eddies reflect from the reattaching shock and form a complex wave pattern. The redeveloping boundary layer seems to be characterized by large–scale eddies.

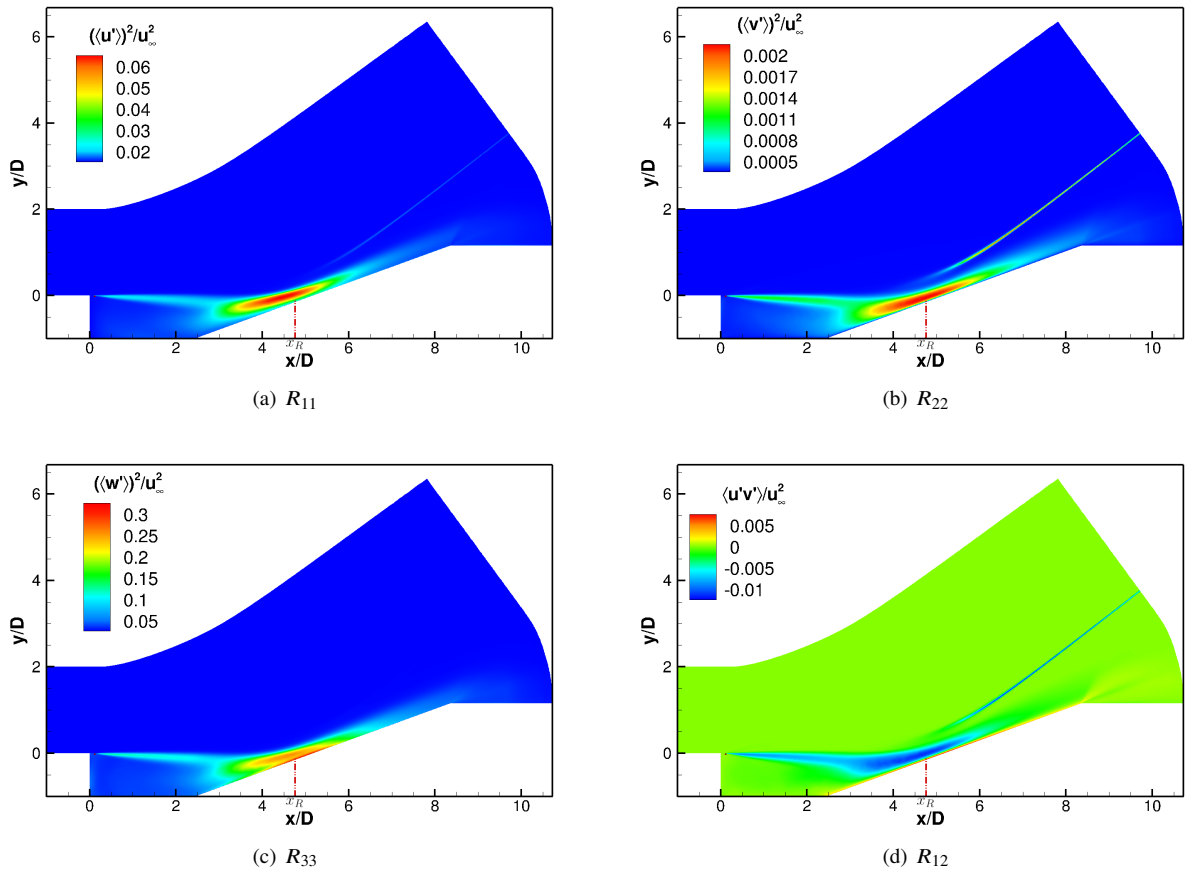

(a) R_{11} (b) R_{22}

(c) R_{33} (d) R_{12}

Fig. 5 Resolved Reynolds stresses.

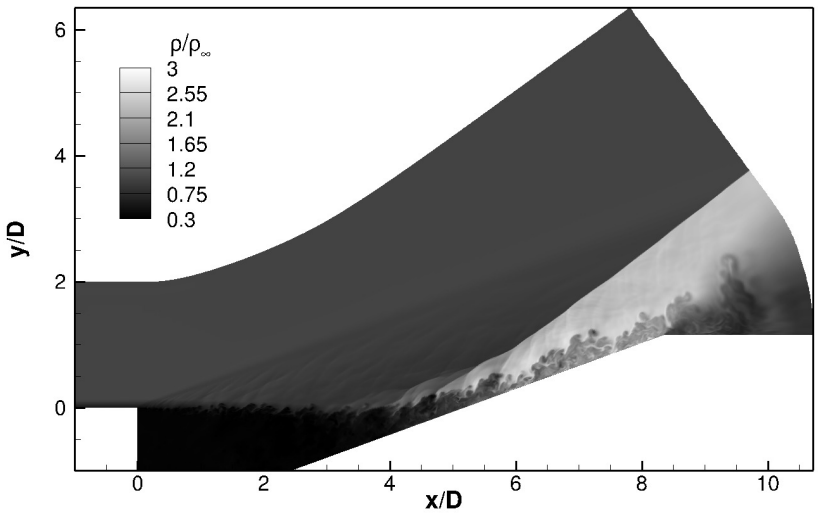

Fig. 6 Instantaneous density contours.

B. Coherent structures

This section discusses the presence of coherent structures in the separated shear layer. It is important to note that in a DES, the initial resolved turbulence structures may be artificial until the flow has broken down to a reasonably resolved turbulence spectrum. With this disclaimer, we report the instantaneous flow structure observed in the shear layer in Fig. 7.

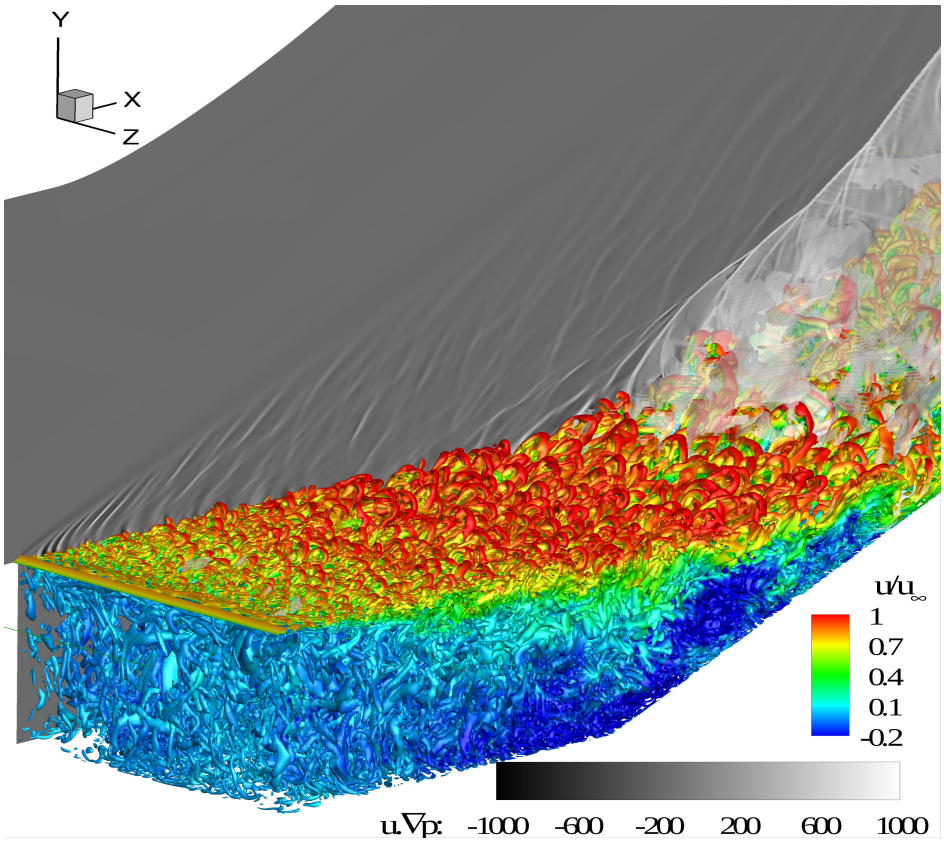

Fig. 7 Three–dimensional flow structures.

In the above figure, the iso–surfaces were created using a constant value of Q–criterion to highlight the vortical structures present in the shear layer. The iso–surfaces are colored with the non–dimensional streamwise velocity magnitude. The slice at the first spanwise index displays the contours of the quantity $\vec{u} \cdot \nabla p$ [21], which is maximum when the velocity vector is aligned with the pressure gradient. Therefore, this quantity highlights regions where a strong pressure gradient is aligned with the flow. The respective colorbars are included in the figure. The reattachment shock is also highlighted using the iso–surface of a constant value of $\vec{u} \cdot \nabla p$.

Lasheras and Choi [22] studied the three–dimensional instability of plane free shear layer, in which the spanwise vortices generated by the Kelvin–Helmholtz instability induce a strain field, thereby stretching the streamwise vorticity of the braids (see Fig. 2) along the principal direction of positive strain. This vorticity field further develops via non–linear interactions such as vortex pairings and tearing. In Fig. 7 the Kelvin–Helmholtz instability at the edge of step seems to generate spanwise uniform vortices, which break down following the process mentioned above. Farther downstream, structures resembling hairpin vortices are observed, which is consistent with the results of Dimotakis and Brown [19] and Samimy et al. [20]. These structures are stacked together in the streamwise direction, analogous to the large scale structures observed by Ganapathisubramani et al. [16] in a Mach 2 turbulent boundary layer.

A quantitative characterization of the large scale structures was done by calculating two–point correlations of fluctuating streamwise velocity on the centerplanes, at zero–time delay. The contours of the correlations are shown in Fig. 8. From Fig. 7, the coherent structures of horseshoe vortices seem lie upstream of the shock. Therefore, the correlations were calculated using two different reference points: one at the midpoint of slice 3 (in Fig. 8(a)) and other at the midpoint slice 4 (in Fig. 8(b)), at approximately the same wall–normal height.

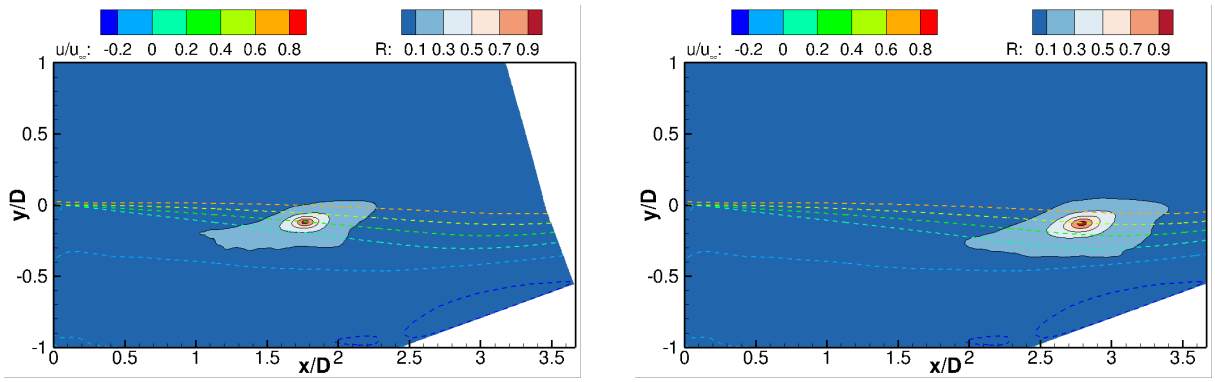

(a) $R_{u'u'}$ (Slice 3). (b) $R_{u'u'}$ (Slice 4).

Fig. 8 Two–point correlations in x–y plane.

For ease of visualization, the correlations are plotted on the centerplane coordinates. The reference points for slice 3 and slice 4 are $(x/D, y/D)_{ref} = (1.77, -0.12)$ and $(x/D, y/D)_{ref} = (2.795, -0.12)$ respectively. The contour lines of mean streamwise velocity are also included for reference. Both the plots are roughly elliptical in shape. The area of correlated region in the case where slice 4 was chosen as the reference is higher. Therefore it seems that the length of the large–scale structure increases downstream as more horse–shoe vortices are stacked together. The approximate length of the structure was calculated from the extremes of the $R = 0.1$ contour line. In terms of the incoming boundary layer thickness, the length of the structure in each case is about $10\delta_\circ$ and $12\delta_\circ$ respectively. Unlike the observations of Ganapathisubramani et al. [16], no regions of negative correlations are observed since the two–point correlations are carried out on an x–y plane instead of an x–z plane. Figure 9 shows the integral time scales calculated from the autocorrelations of streamwise velocity fluctuations at each grid point on the centerplanes. In this figure, results are shown for slices 3–5 and mean velocity contour lines are superimposed and labeled for reference. The integral time scale is maximum for a small localized region above the contour line $u/u_\infty = 0$. Overall, contour values of high time scales lie within the shear layer. This might be joint result of the high residence time associated with large–scale structures in Fig. 8 and low–frequency shear layer flapping, which is discussed in Sec. III.C and III.D. The time–scale decreases towards the center of the shear layer and in the separation bubble, indicating high frequency events at those locations.

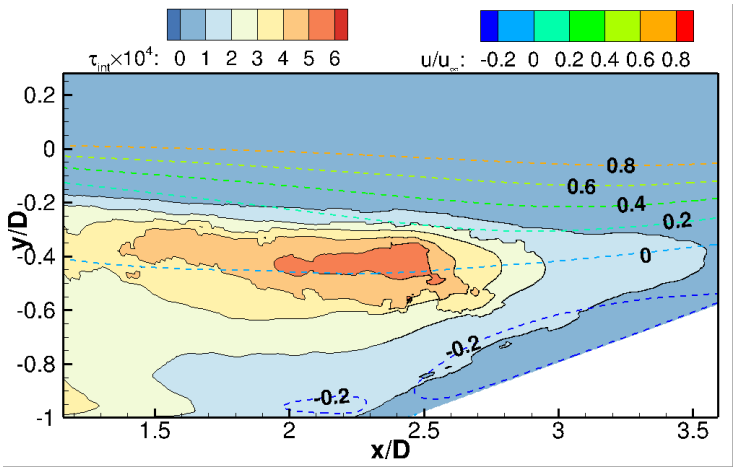

Fig. 9 Integral time scales.

Figure 10 shows two–point correlations at position 1 on the ramp. This array of locations lies upstream of the mean reattachment point and within the recirculation zone. Recall that data on the ramp was extracted at seven equidistant spanwise locations, sampled at a higher frequency. To construct Fig. 10(a), the data on the ramp was read as a mesh, under–resolved in the spanwise direction. The reference point in this case was the midpoint of the centerline

$(x/D, z/D)_{ref} = (3.03, 0)$ and wall pressure fluctuations were used as the variable.

The resulting plot is elliptical with a wide area of correlation in the spanwise direction. Absence of any negative values indicates velocity fluctuations oriented in the same direction. This is a sign of a large vortex that was observed by Kiya and Sasaki [23] which was periodically shed from the separation bubble. The vortex shedding frequency was higher than low–frequency flapping of the shear layer in their studies. This observation is consistent with the plot of integral time scale in Fig. 9. Figure 10(b) shows two–point correlations on the centerplanes using pressure fluctuations. The reference signal was constructed using wall pressure fluctuations at $x/D = 2.75$. The resulting plot indicates large–scale vortices with a wall normal extent of $y/D \approx 0.24$. Farther downstream at position 2 (in Fig. 10(c)) and position 3 (in Fig. 10(d) on the ramp surface, the correlations become significantly narrower. The corresponding locations lie either very close to or downstream of the mean reattachment point. The correlations in Fig. 10(c) may point towards the eddies in the shear layer, before it reattaches. The plot in Fig. 10(d) is typical of near wall structures in a boundary layer.

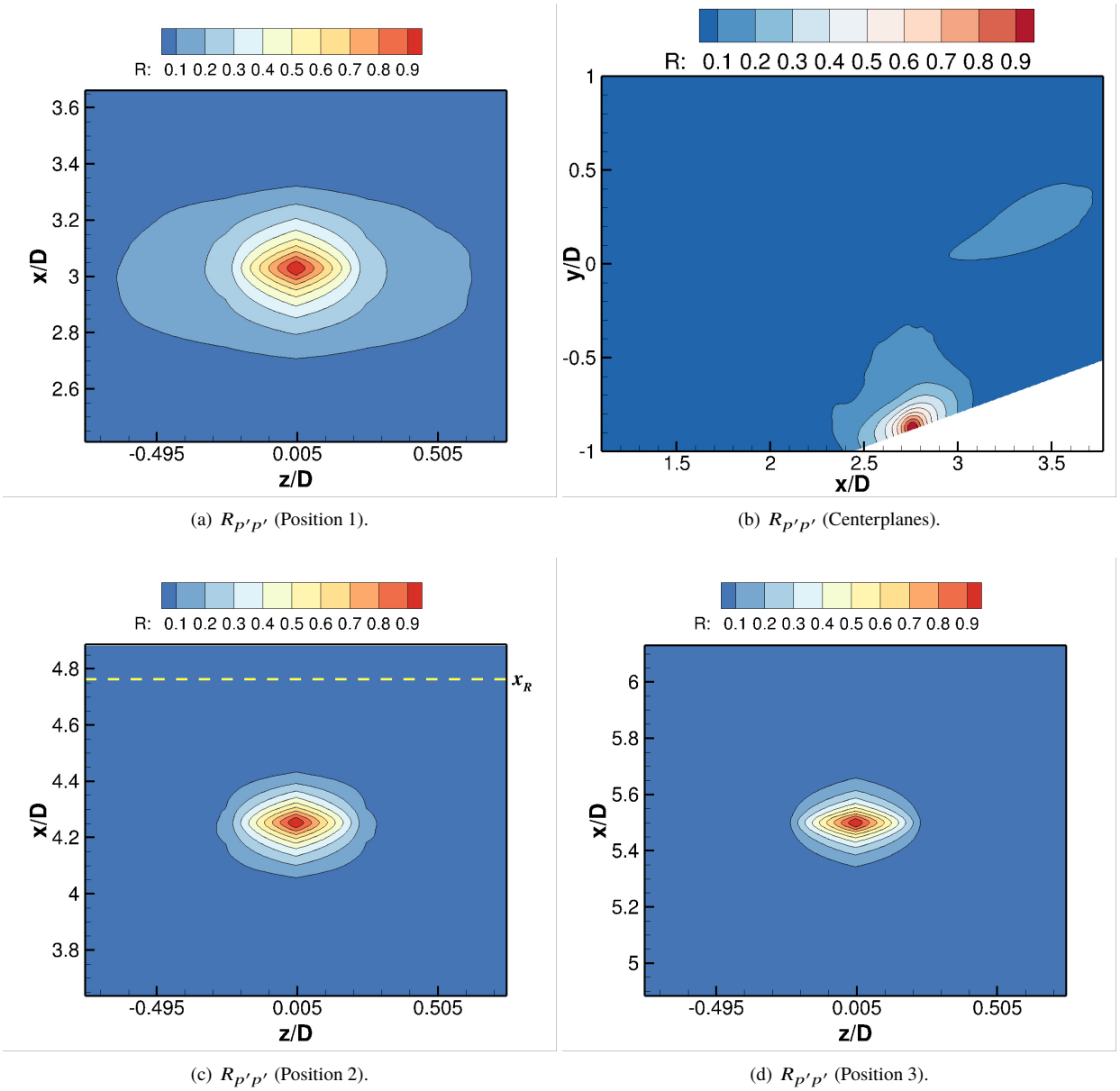

(a) $R_{p'p'}$ (Position 1).

(b) $R_{p'p'}$ (Centerplanes).

(c) $R_{p'p'}$ (Position 2).

(d) $R_{p'p'}$ (Position 3).

Fig. 10 Two–point correlations on the ramp.

C. Unsteadiness of the interaction

Based on previous work in reattaching shear layers and turbulent separation bubbles, the main contributing factors to the unsteadiness of the interaction are: shear layer flapping, breathing the of separation bubble, and vortex shedding from the shear layer. Based on the interaction, coupling may occur between all the three or any of the two factors. This section investigates the unsteady mechanisms present in the current flowfield using spectral plots. We start by studying the streamwise variation of spectra of wall pressure fluctuations. Although the centerplanes are undersampled as compared to lines along the ramp surface, they are used to extract the data as they span the entire domain. Figure 11 shows the premultipled spectra of wall pressure fluctuations at six streamwise stations, plotted against the non-dimensional Strouhal number. The choice of length scale to calculate the Strouhal number poses a conundrum. There are many options such as the interaction length L_i, the cavity length L_c, the mean reattachment length x_R, and the step height D. For this study, the choice of the length scale was made after referring to the results from previous studies.

Figure. 11(a) shows the spectra close to the step at $x/D = 0.394$ with two distinct peaks. Based on similar observations by Kiya and Sasaki [23] as well as Hiller and Cherry [24], the peak at lower Strouhal number is a signature of shear–layer flapping near the separation point. The second peak at the higher frequency corresponds to the eddies present in the separation bubble. To determine the appropriate length scale, the frequencies were scaled by the mean reattachment length x_R and the cavity length L_c. The Strouhal number corresponding to the peak at lower frequency in each case was $fx_R/u_\infty = 0.32$ and $fL_c/u_\infty = 0.16$ respectively. The non–dimensional flapping frequency observed in Kiya and Sasaki's [23] experiment on a blunt flat plate was $fx_R/u_\infty \approx 0.12$. In Eaton and Johnston's [12] experiment on a backward facing step, they observed 30% of the measured turbulence intensity occurring below $fx_R/u_\infty \approx 0.15$, which is close to the result of Kiya and Sasaki [23]. Hence in order to be in the same ballpark of the previous values, L_c was chosen as the desired length scale. Given the difference in geometries between the current study and previous experiments and lack of previous literature on unsteadiness of compressible reattaching shear layers, the authors feel that this choice is a valid starting point. Based on the chosen length scale, the energy associated with flapping is concentrated at frequencies $fL_c/u_\infty \lessapprox 1$.

Although the current results are close to values in previous studies, the authors acknowledge that the compressible nature of this flowfield might have an impact on the shear layer flapping. Eaton and Johnston [12] point out that instantaneous imbalance between the shear layer entrainment from the recirculating zone and reinjection of fluid near the reattachment may be a possible cause of the low–frequency shear layer flapping. Based on previous studies [25, 26], it is known that compressible shear layers have lower growth and entrainment rate as compared to incompressible shear layers. These two observations may affect the low–frequency flapping of the shear layer. Another possibility lies in the amplified feedback from the reattachment shock on the ramp. It is well known that shock–wave/boundary–layer interactions are characterized by low–frequency motion of the shock foot [1–3]. Therefore the disturbances amplified by the shock wave may propagate upstream through the subsonic portion of the recirculation bubble and modulate the shear layer flapping at the separation point. No shocks were present in the detailed studies carried out on turbulent separation bubbles [12, 23, 24]. Also, a combined effect of compressibility of the shear layer and amplification by the reattachment shock can be expected to change the flapping characteristics. These avenues serve as topics for future study.

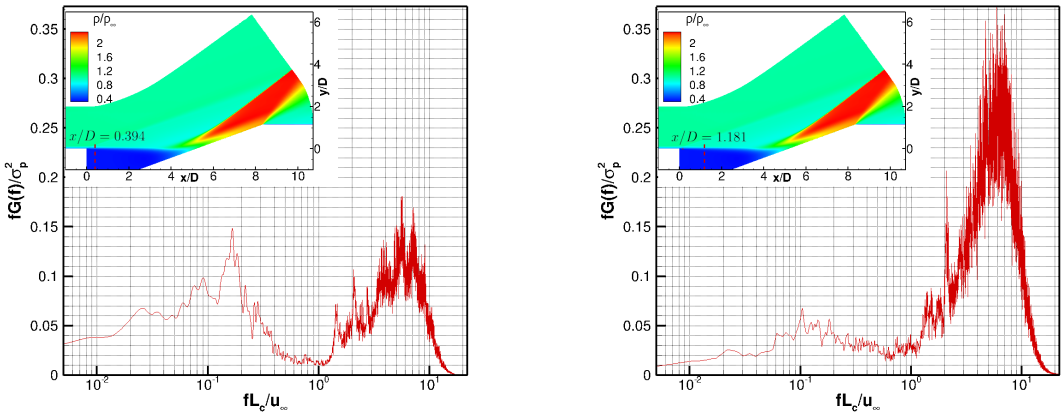

(a) $x/D = 0.394$

(b) $x/D = 1.181$

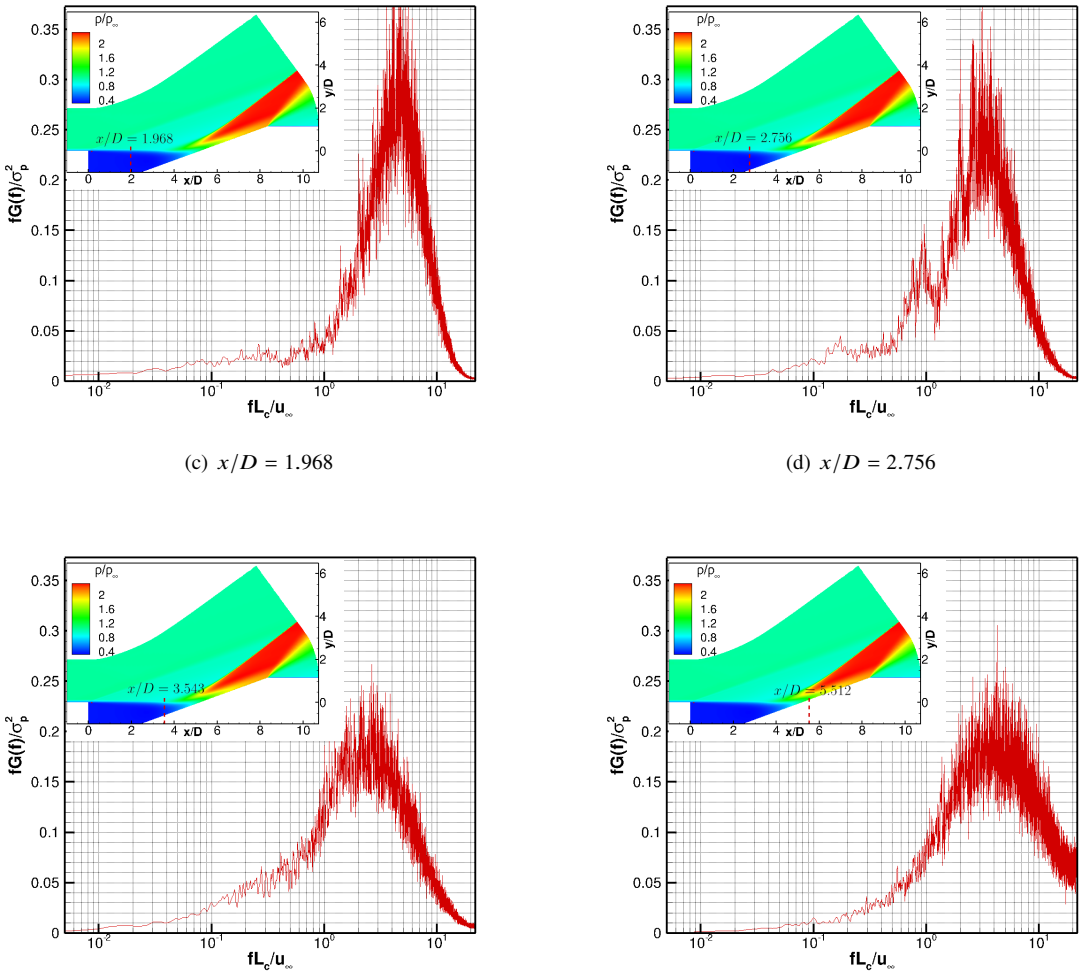

(c) $x/D = 1.968$

(d) $x/D = 2.756$

(e) $x/D = 3.543$

(f) $x/D = 5.512$

Fig. 11 Pre-multiplied wall pressure spectra.

The spectra shown henceforth are plotted against non–dimensional frequency scaled by L_c. Figure 11(b) shows the spectra slightly downstream at $x/D = 1.181$. The peak at $fL_c/u_\infty \approx 0.16$ has decreased in magnitude which is accompanied by an increase in the peak at the higher non–dimensional frequency. At $x/D = 1.968$ in Fig. 11(c), the peak at lower–frequency has completely disappeared, indicating most of the energy is distributed in the turbulence of the separation bubble at higher frequencies. The spectra in Fig. 11(d) lies close to the ramp corner at $x/D = 2.756$. A small peak at $fL_c/u_\infty \approx 0.962$ is observed. This peak might correspond to the large scale vortices in the separation bubble observed by Kiya and Sasaki [23]. The correlation plots in Fig. 10(a) and 10(b) support this hypothesis. At $x/D = 3.543$, energy transfer to lower frequencies take place with no distinct peak present. This may be a result of the unsteady reattachment shock motion. Farther downstream at $x/D = 5.512$ which lies downstream of the mean reattachment location, the energy spectra is broadband in nature.

Determination of reattachment shock motion was difficult for this flowfield as, unlike a compression ramp or an incident shock–wave/boundary–layer interaction (SBLI), the reattachment shock foot was composed of multiple compression waves and weak shocks. Therefore the conventional pressure threshold methods were not effective in determining the shock location history. Here the lowest frequency detected was associated with shear layer flapping. Figure 12 shows spectral plots obtained from data on the ramp surface at four streamwise stations, which were sampled at a higher frequency than the centerplanes. The spectral density function $G(f)$ is normalized by the square of rms of pressure fluctuations σ_p.

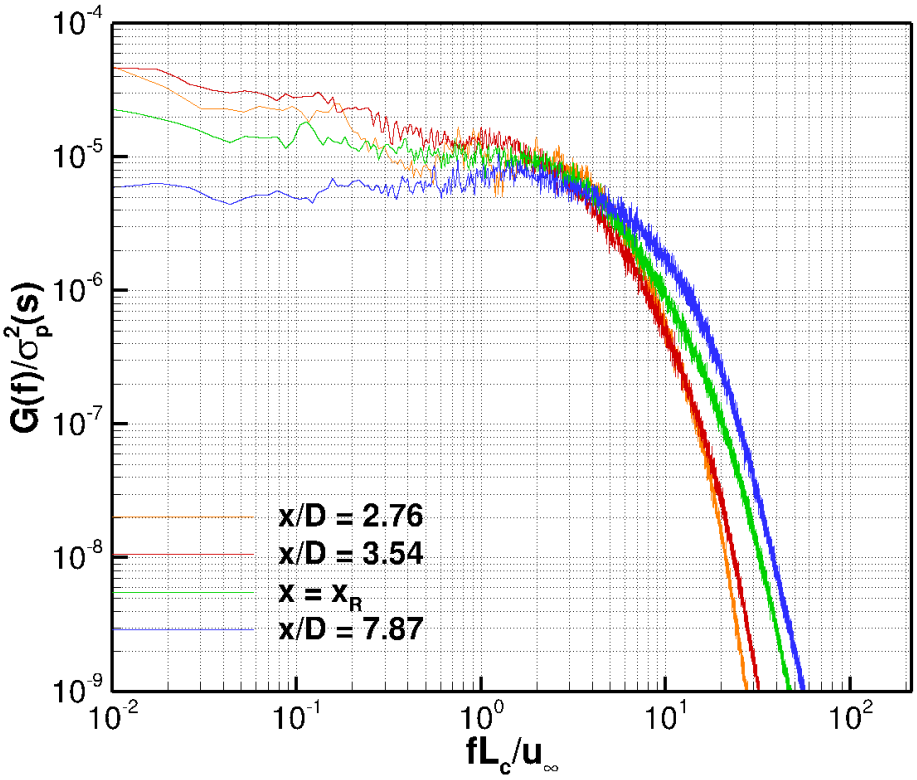

Fig. 12 Spectra of wall–pressure fluctuations on the ramp.

From the figure above, increase of energy content at lower frequencies occurs between streamwise stations $x/D = 2.756$ and $x/D = 3.543$. Close to the time–mean reattachment point, the energy content at lower frequencies decreases significantly. Farther downstream, most of the energy is contained in the turbulence of the redeveloping boundary layer. Based on the nature of this spectral plot, it seems that the low–frequency motion is dominant in the range $3.543 \lessapprox x/D \lessapprox x_R$.

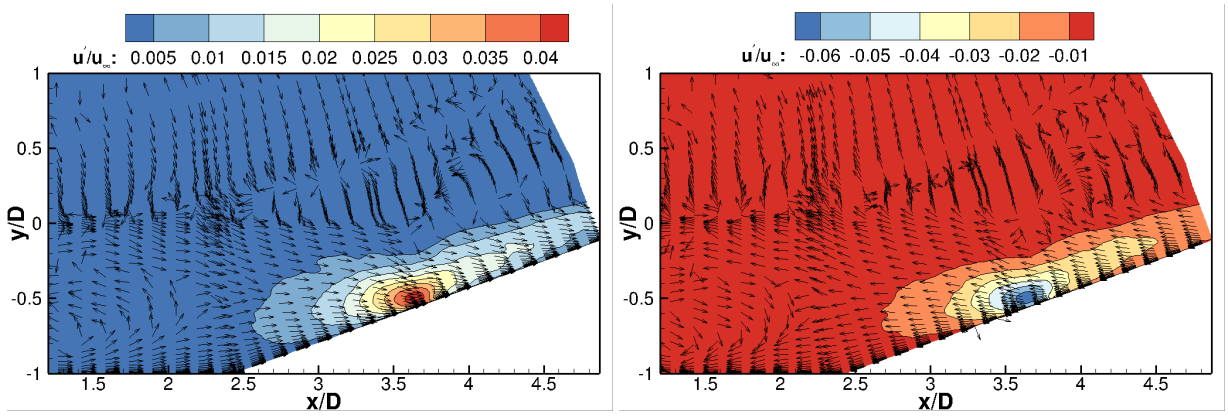

(a) $\tilde{x}_R < x_R$. (b) $\tilde{x}_R > x_R$.

Fig. 13 Conditional averages (mean subtracted).

Conditional averages based on the instantaneous location of the reattachment point with respect to its time–mean were carried out. The instantaneous reattachment point was chosen based on the sign of skin–friction coefficient at that

time. The conditionally–averaged streamwise velocity fluctuations are shown in Fig. 13. The conditionally averaged vector fields are also superimposed on each figure. The term $\tilde{x}_R$ denotes instantaneous reattachment location.

In Fig. 13(a) when the instantaneous reattachment lies upstream of its time–mean value, the streamwise velocity fluctuations are positive. The vector field indicates a negative wall–normal velocity. This is most likely caused due to the downward motion of the shear layer, which results in the upstream movement of the instantaneous reattachment location. The positive streamwise velocity fluctuations may correspond to the region downstream of the large–scale vortex shed from the recirculation bubble. In Fig. 13(b) when the instantaneous reattachment location lies downstream of its time–mean value, the streamwise velocity fluctuations are negative. The vector fields show an upwash on account of positive wall–normal velocity and an upward motion of the shear layer - which causes the reattachment point to move downstream. The negative streamwise velocity fluctuations indicate increase in the separation extent. Note that the higher values of conditionally averaged velocity contours are localized in the region $3 \lessapprox x/D \lessapprox 4.5$. Therefore it seems that the shear layer flapping affects the fluctuating quantities in that range. This explains the increase in energy at low frequencies in the spectra at $x/D = 3.54$ (see Fig. 11(e) and 12), which excludes the possibility of reattachment shock motion affecting that range.

D. Shear layer flapping

In the previous section, the low–frequency flapping the of shear layer was quantified. This sections shows a visual representation of the same. The velocity signals on the centerplane were low–pass filtered at in time every grid point. From Fig. 11(a), the energy associated with the flapping is concentrated at frequencies $fL_c/u_\infty \leq 1$. Using this relation, the passband frequency for the low–pass filter was determined. The filtered velocity fields were then used to make a movie* that distinctly showed the vertical movement of the shear layer and breathing of the separation bubble. Due to computer memory constraints, an additional 100 time steps between each time instant were skipped. The corresponding time step between successive frames is $\Delta t = 0.25$ ms. A few frames of streamwise velocity are shown in Fig. 14.

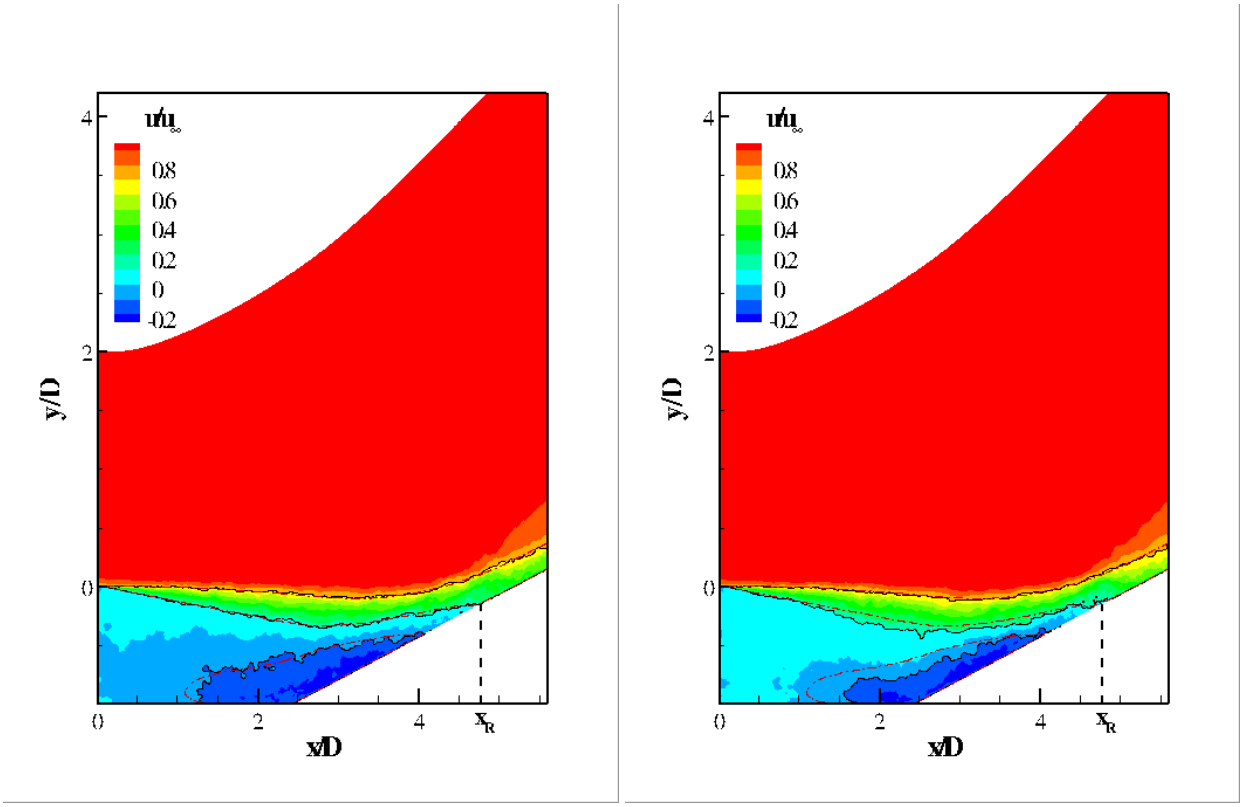

(a) $t = 3.75$ ms (b) $t = 82.5$ ms

*present at https://engineering.purdue.edu/~jpoggie/RSL/movie_lp.mp4

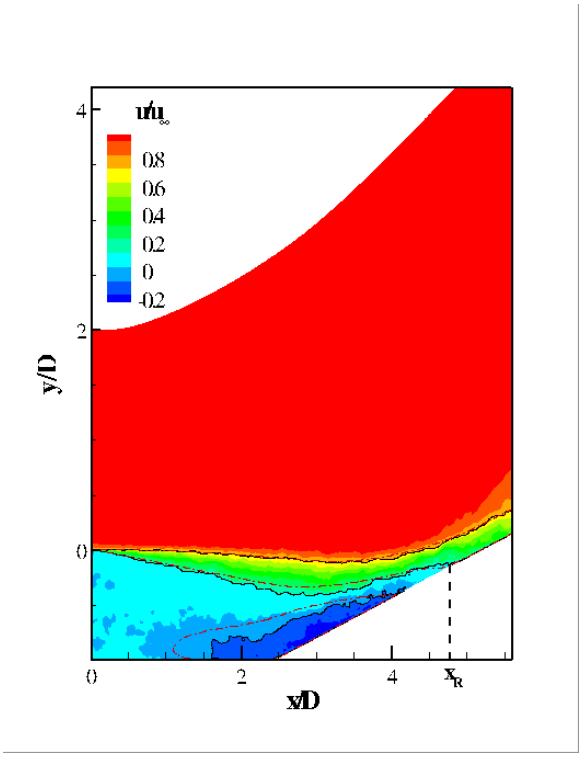

(c) t = 128.75 ms

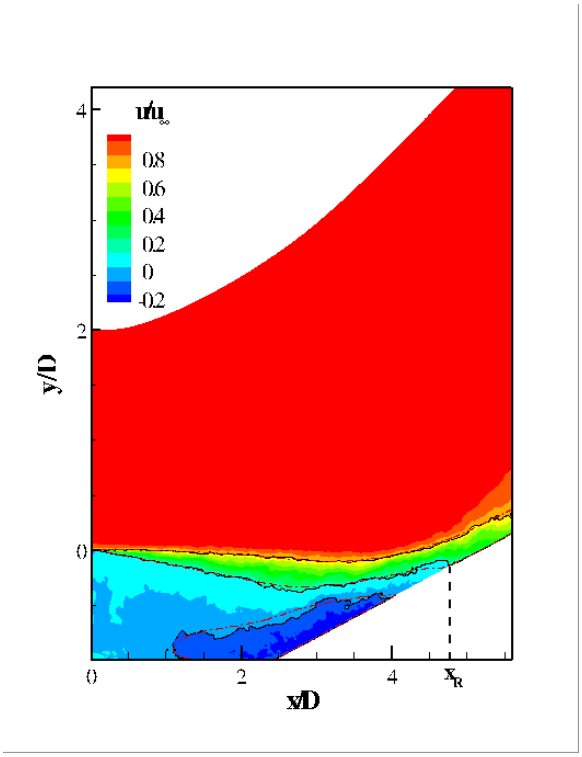

(d) t = 150 ms

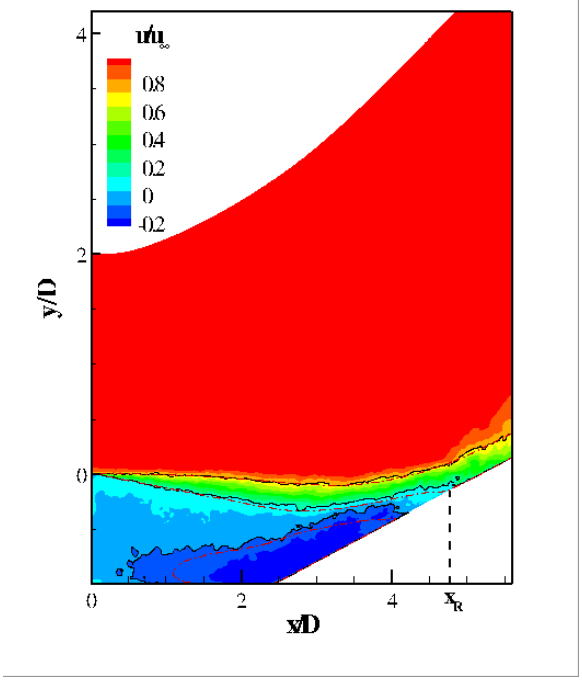

(e) t = 196.25 ms

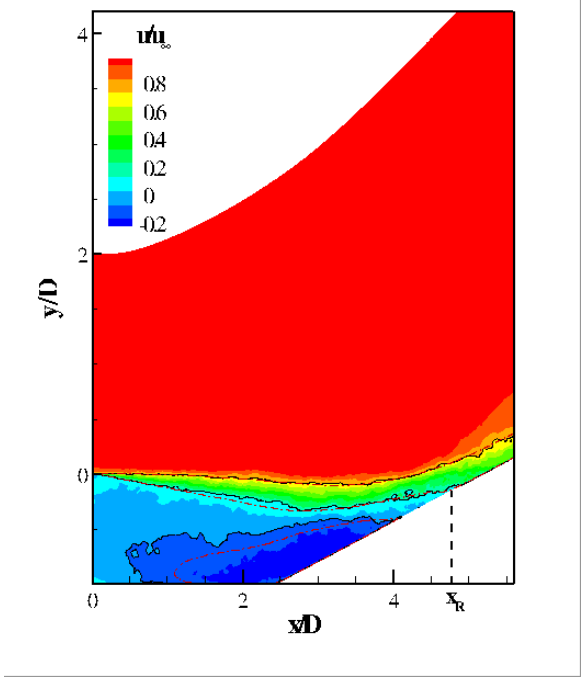

(f) t = 265 ms

Fig. 14 Flapping of the shear layer.

Note that the pictures shown above were chosen based on the events they illustrated, and not corresponding to even spacing in time. In the above figures, three contour levels: $u/u_\infty = 0.7$, $u/u_\infty = 0.15$, and $u/u_\infty = -0.2$ are highlighted. These three contour levels will referred to as C1, C2, and C3 respectively. The black solid lines are instantaneous contour lines and the red dotted lines are the respective time–mean values. The mean reattachment location is also highlighted. In Fig. 14(a), the separation bubble and the shear layer are approximately at their mean position with contour line at C2 ending approximately at the reattachment location. The separation bubble (contour line at C3) shrinks at $t = 82.5$ ms (see Fig. 14(b)) and the contour line at C2 moves below its mean position, indicating a downward movement of the shear layer. Notice the slight decrease separation extent and upstream movement of the instantaneous reattachment point. The contour line at C1 does not show significant movement from its mean. Figure 14(c) shows a similar event at $t \approx 129$ ms, but separation bubble shrinks to a different position.

At $t = 150$ ms (see Fig. 14(d)), the contour lines are approximately at the mean position. Figures 14(e) and 14(f) show the expansion of the separation bubble. The contour line at C2 moves above its means position indicating an upward movement of the shear layer. This upward movement slightly increases the separation extent. Notice that upward/downard movement of the contour line at C2 is not observed close to the step. A possible reason for this can be attributed to undersampling of the frames, thereby not providing enough time–resolution to resolve the low–frequency motion at the separation point. Also, resolved turbulence does not appear in the solution until somewhat downstream of the step. As expected, the contour line at C1 remains at its mean position. From these figures, the shrinking and expansion of the separation bubble is determined to be asymmetric and aperiodic. Also the response of the shear layer to the breathing of the separation bubble suggests that the latter is the driving force of shear layer flapping, which agrees with the results of Ma and Schröder [14].

IV. Conclusions

Results from the numerical calculations of unsteadiness in a compressible reattaching carried out by Leger et al. [7] were analyzed using statistical techniques. The mean flow results showed formation of reattachment shock with a complex shock foot and a large recirculation vortex. The trend of resolved Reynolds stresses agreed with the experimental results of Hayakawa et al. [10]. The instantaneous flowfields displayed complex flow features such as radiation of acoustic waves from the eddies, increase in turbulent length scales post reattachment, and formation of long structures composed of horseshoe vortices in the shear layer, upstream of the reattachment shock. Two–point correlations of u–velocity and wall–pressure fluctuations on the x–y and x–z planes confirmed this observation, as well as indicated a large vortex at the beginning of the ramp and in the separated zone. This result is consistent with the experiments of Kiya and Sasaki [23]. These coherent structures were further quantified by calculation of integral time scales from the autocorrelation plots of streamwise velocity fluctuations.

Wall pressure spectra were plotted to study the unsteadiness of the interactions. Close to the step, the premultiplied spectra was bimodal, with the peak at lower frequency corresponding to the shear layer flapping. Conditionally averaged velocity field showed a correlation between the shear–layer flapping and the oscillation of instantaneous reattachment point about its mean. The filtered velocity field represented the flapping motion and breathing of the separation bubble. Based on the frames, the breathing of the separation bubble interacts with the flapping of the shear layer and change in the separation extent. The response of the shear layer to the breathing of the bubble decreases progressively away from the wall.

Although the unsteadiness of this interactions was quantified, there are many questions that remain unanswered. An amplified feedback from the shock can travel upstream through the subsonic portion of the separation bubble to modulate the motion of the shear layer at the separation point, roughly analogous to Rossiter modes observed in open cavities. The effect of these factors on the overall unsteadiness of the interactions is not yet known. Novel methods to track the reattachment shock motion need to be designed in order to study its spectral characteristics. The authors are working on performing modal decomposition of the flowfield to address these issues.

Acknowledgements

The authors are grateful to Dr. T. Leger for providing the computational data analyzed in this study. This work was supported in part by the U.S. Air Force Office of Scientific Research grant FA9550-17-1-0153, monitored by I. Leyva.

References

[1] Clemens, N. T., and Narayanaswamy, V., "Low-frequency unsteadiness of shock wave/turbulent boundary layer interactions," *Annual Review of Fluid Mechanics*, Vol. 46, 2014, pp. 469–492.

[2] Dolling, D. S., "Fifty years of shock-wave/boundary-layer interaction research: what next?" *AIAA Journal*, Vol. 39, No. 8, 2001, pp. 1517–1531.

[3] Gaitonde, D. V., "Progress in shock wave/boundary layer interactions," *Progress in Aerospace Sciences*, Vol. 72, 2015, pp. 80–99.

[4] Poggie, J., and Smits, A. J., "Experimental Evidence for Plotkin Model of Shock Unsteadiness in Separated Flow," *Physics of Fluids*, Vol. 17, 2005, 018107.

[5] Touber, E., and Sandham, N. D., "Low-Order Stochastic Modelling of Low-Frequency Motions in Reflected Shock-Wave / Boundary-Layer Interactions," *Journal of Fluid Mechanics*, Vol. 671, 2011, pp. 417–465.

[6] Nichols, J. W., Larsson, J., Bernardini, M., and Pirozzoli, S., "Stability and Modal Analysis of Shock / Boundary Layer Interactions," *Theortical and Computational Fluid Dynamics*, Vol. 31, 2017, pp. 33–50.

[7] Leger, T., Bisek, N., and Poggie, J., "Detached-Eddy Simulation of a Supersonic Reattaching Shear Layer," *AIAA Journal*, Vol. 55, No. 11, 2017, pp. 1–12.

[8] Poggie, J., and Smits, A. J., "Large-scale structures in a compressible mixing layer over a cavity," *AIAA Journal*, Vol. 41, No. 12, 2003, pp. 2410–2419.

[9] Settles, G. S., Williams, D. R., Baca, B. K., and Bogdonoff, S. M., "Reattachment of a compressible turbulent free shear layer," *AIAA Journal*, Vol. 20, No. 1, 1982, pp. 60–67.

[10] Hayakawa, K., Smits, A. J., and Bogdonoff, S. M., "Turbulence measurements in a compressible reattaching shear layer," *AIAA Journal*, Vol. 22, No. 7, 1984, pp. 889–895.

[11] Poggie, J., and Smits, A., "Shock unsteadiness in a reattaching shear layer," *Journal of Fluid Mechanics*, Vol. 429, 2001, pp. 155–185.

[12] Eaton, J. K., and Johnston, J. P., "Low frequency unsteadiness of a reattaching turbulent shear layer," *Turbulent Shear Flows 3*, Springer, 1982, pp. 162–170.

[13] Eaton, J. K., and Johnston, J. P., "A review of research on subsonic turbulent flow reattachment," *AIAA Journal*, Vol. 19, No. 9, 1981, pp. 1093–1100.

[14] Ma, X., and Schröder, A., "Analysis of flapping motion of reattaching shear layer behind a two-dimensional backward-facing step," *Physics of Fluids*, Vol. 29, 2017, 115104.

[15] Ganapathisubramani, B., Clemens, N., and Dolling, D., "Effects of upstream boundary layer on the unsteadiness of shock-induced separation," *Journal of Fluid Mechanics*, Vol. 585, 2007, pp. 369–394.

[16] Ganapathisubramani, B., Clemens, N., and Dolling, D., "Large-scale motions in a supersonic turbulent boundary layer," *Journal of Fluid Mechanics*, Vol. 556, 2006, pp. 271–282.

[17] Brown, G. L., and Roshko, A., "On density effects and large structure in turbulent mixing layers," *Journal of Fluid Mechanics*, Vol. 64, No. 4, 1974, pp. 775–816.

[18] Bernal, L. P., and Roshko, A., "Streamwise vortex structure in plane mixing layers," *Journal of Fluid Mechanics*, Vol. 170, 1986, pp. 499–525.

[19] Dimotakis, P. E., and Brown, G. L., "The mixing layer at high Reynolds number: large-structure dynamics and entrainment," *Journal of Fluid Mechanics*, Vol. 78, No. 3, 1976, pp. 535–560.

[20] Samimy, M., Reeder, M., and Elliott, G., "Compressibility effects on large structures in free shear flows," *Physics of Fluids*, Vol. 4, No. 6, 1992, pp. 1251–1258.

[21] Gonzalez, D. R., Adler, M. C., and Gaitonde, D. V., "Temporal Evolution of Dynamical Structures in a Swept Compression Ramp," AIAA Paper 2018-4034, American Institute of Aeronautics and Astronautics, Atlanta, GA, June 2018.

[22] Lasheras, J., and Choi, H., "Three-dimensional instability of a plane free shear layer: an experimental study of the formation and evolution of streamwise vortices," *Journal of Fluid Mechanics*, Vol. 189, 1988, pp. 53–86.

[23] Kiya, M., and Sasaki, K., "Structure of a turbulent separation bubble," *Journal of Fluid Mechanics*, Vol. 137, 1983, pp. 83–113.

[24] Hillier, R., and Cherry, N., "Pressure fluctuations under a turbulent shear layer," *Proc. 3rd Symp. on Turbulent Shear Flows*, 1981, pp. 16–23.

[25] Samimy, M., and Elliott, G., "Effects of compressibility on the characteristics of free shear layers," *AIAA Journal*, Vol. 28, No. 3, 1990, pp. 439–445.

[26] Elliott, G., and Samimy, M., "Compressibility effects in free shear layers," *Physics of Fluids*, Vol. 2, No. 7, 1990, pp. 1231–1240.